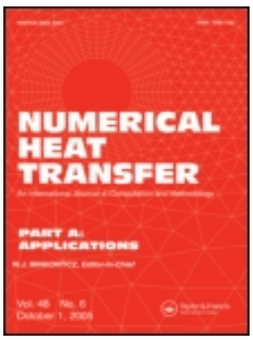

Numerical Heat Transfer, Part A: Applications

ISSN: 1040-7782 (Print) 1521-0634 (Online) Journal homepage: http://www.tandfonline.com/loi/unht20

Laminar Natural Convection in a Horizontal Rhombic Annulus

F. Moukalled , H. Diab & S. Acharya

To cite this article: F. Moukalled , H. Diab & S. Acharya (1993) Laminar Natural Convection in a Horizontal Rhombic Annulus, Numerical Heat Transfer, Part A: Applications, 24:1, 89-107, DOI: 10.1080/10407789308902604

To link to this article: http://dx.doi.org/10.1080/10407789308902604

Published online: 16 Jan 2007.

Numerical Heat Transfer, Part A, vol. 24, pp. 89–107, 1993

LAMINAR NATURAL CONVECTION IN A HORIZONTAL RHOMBIC ANNULUS

F. Moukalled and H. Diab
Faculty of Engineering and Architecture, American University of Beirut, Beirut, Lebanon

S. Acharya
Mechanical Engineering Department, Louisiana State University, Baton Rouge, Louisiana 70803

This paper presents the simulation of heat transfer and flow patterns in an enclosure between two isothermal concentric cylinders of rhombic cross sections. Four different values of the enclosure gap (E_g = 0.875, 0.75, 0.5, and 0.25) and three different rhombic angles (Ω = 10°, 20°, and 30°) are considered. At low Rayleigh numbers (10^3–10^5) the flow is weak and conduction is the dominant mode of heat transfer. Convection plays a key role starting at higher Rayleigh numbers (10^6–10^7). For all cases studied, there is no tendency for flow separation at the horizontal corners. The flow strength is found to increase with increasing rhombic angle, increasing enclosure gap and increasing Rayleigh number. The critical Rayleigh number at which the heat transfer is influenced by convection decreases with increasing gap values and increasing rhombic angle; it is as high as 10^6–10^7 for E_g = 0.25 and decreases to about 10^4 for E_g = 0.875.

INTRODUCTION

Natural convection in enclosures has received considerable attention in recent years due to the many important applications that involve natural convection processes. Ostrach [1] has recently reviewed the work on natural convection in simple enclosures and cylindrical annuli. Work reported in more complex geometries has been rather limited. The focus of the present study is on natural convection heat transfer in an annulus between two rhombic bodies.

Natural convection in the annuli between concentric and eccentric horizontal cylinders has been reasonably well studied. Kuehn and Goldstein [2] studied numerically and experimentally the laminar flow of air and water within a horizontal annulus and provided an excellent survey of the previous research done in this area. More recent studies on natural convection between cylindrical annuli include those of Castrejon and Spalding [3], Kumar [4], and Kolesnikov and Bubnovich [5].

Cho et al. [6] numerically studied natural convection between eccentric horizontal cylindrical annuli and demonstrated that for very small eccentricity the overall thermal behavior of the annuli is similar to that in exactly concentric cylinders. Prusa and Yao [7] studied annuli with large eccentricity and noted the

The help of Wissam Ali Ahmad and Rami Debouk in computer work, and the financial support provided by the University Research Board of the American University of Beirut through grant 18-4217, are gratefully acknowledged.

1040–7782/93 $10.00 + .00

NOMENCLATURE

$a_P^\phi, a_E^\phi, a_W^\phi, a_N^\phi, a_S^\phi$	coefficients in the finite difference equation
$b_o^\phi, b_{no}^\phi, b_p^\phi$	source term, source term due to nonorthogonality, and source term due to pressure gradient
c_p	specific heat of fluid
E_g	dimensionless enclosure gap $[= (L_o - L_i)/L_i]$
g	acceleration due to gravity
G_1, G_2	convective terms normal to grid cell boundaries ($G_1 = UY_\eta - VX_\eta$, $G_2 = VX_\xi - UY_\xi$)
$h, \bar{h}$	local and average coefficient of convection heat transfer
J	Jacobian $(= X_\xi Y_\eta - X_\eta Y_\xi)$
k	thermal conductivity
L	length of pipe's main diagonal
Nu	local Nusselt number $(= hL/k)$
$\overline{Nu}$	average Nusselt number $(= hL/k)$
p, P	thermodynamic pressure, dimensionless pressure $[P = (p + \rho gy)/\rho(\nu/L_o)^2]$
Pr	Prandtl number $(= \mu c_p/k)$
Ra	Rayleigh number $[= g\beta(T_h - T_c)L_o^3/\nu\alpha]$
S^ϕ	source term
T	dimensional temperature
u, U	dimensional and dimensionless velocity in x direction $[U = u(\nu/L_o)]$
v, V	dimensional and dimensionless velocity in y direction $[V = v(\nu/L_o)]$
x, X	dimensional and dimensionless coordinate along the horizontal direction $(X = x/L_o)$
y, Y	dimensional and dimensionless coordinate along the vertical direction $(Y = y/L_o)$
α, β, γ	metric quantities $(\alpha = X_\eta^2 + Y_\eta^2$, $\beta = X_\xi X_\eta + Y_\xi Y_\eta$, $\gamma = X_\xi^2 + Y_\xi^2)$
β_T	coefficient of thermal expansion
Γ^ϕ	diffusion coefficient
$\delta\xi, \delta\eta$	grid point spacing in ξ and η directions
$\Delta\xi, \Delta\eta$	control volume spacing in ξ and η directions
η, ξ	transformed coordinate
θ	dimensionless temperature $[= (T - T_c)/(T_h - T_c)]$
ν	kinematic viscosity
ρ	density
ϕ	dependent variable
Ψ	stream function
Ω	rhombic angle

Subscripts

c	cold wall
e, n, s, w	refers to control volume faces; n also refers to the normal direction
h	hot wall
i	condition at inner pipe
l	lower part $(0 < s/s_{max} \leq 0.5)$
max	maximum value
o	condition at outer pipe
P, E, N, S, W	refers to grid points
u	upper part $(0.5 < s/s_{max} \leq 1)$

Superscripts

ϕ	refers to dependent variable
*	previous iteration value
'	correction value

significant influence of eccentricity on the heat transfer and the flow field. Ho and Lin [8] and Nayor et al. [9] have also studied natural convection between eccentric cylinders. Chang et al. [10] used the Galerkin finite element method to analyze natural convection heat transfer around a square cylinder placed concentrically in a horizontal circular cylinder. Results, verified experimentally, indicated the absence of any boundary layer separation past the sharp edges of the inner cylinder in the range of Rayleigh numbers considered. Lee and Lee [11] examined the heat transfer characteristics in the annuli between confocal elliptic cylinders. Heat transfer measurements in a parallelogrammic enclosure were reported by Seki

et al. [12], and the dependence of the heat transfer coefficient on the enclosure tilt angle was shown. Boyd [13] reported heat transfer experiments for natural convection in a horizontal annulus with a hexagonal inner body and a circular outer body. The application of interest in their study was heat transfer in a cask used for shipping spent nuclear fuel.

The objective of this paper is to present numerical solutions for natural convection in the annulus between two horizontal concentric pipes of rhombic cross sections (Fig 1). The flow is driven by buoyancy forces arising from the difference in temperature between the heated inner and cooled outer isothermal walls that are maintained at temperature T_h and T_c, respectively. Solutions, with air as the working fluid, are presented for a wide range of Rayleigh numbers and geometric parameters.

GOVERNING EQUATIONS

The flow is assumed to be steady, laminar, and two-dimensional. Density variation is modeled by using the Boussinesq approximation, according to which

$$\rho = \rho_0[1 - \beta_T(T - T_0)] \tag{1}$$

where ρ, ρ_0, T, T_0, and β_T are the density, reference density, temperature, reference temperature, and coefficient of thermal expansion, respectively. For small and moderate temperature differences, the Boussinesq assumption has been shown to be adequate, and radiation effects can be assumed to be small. With the

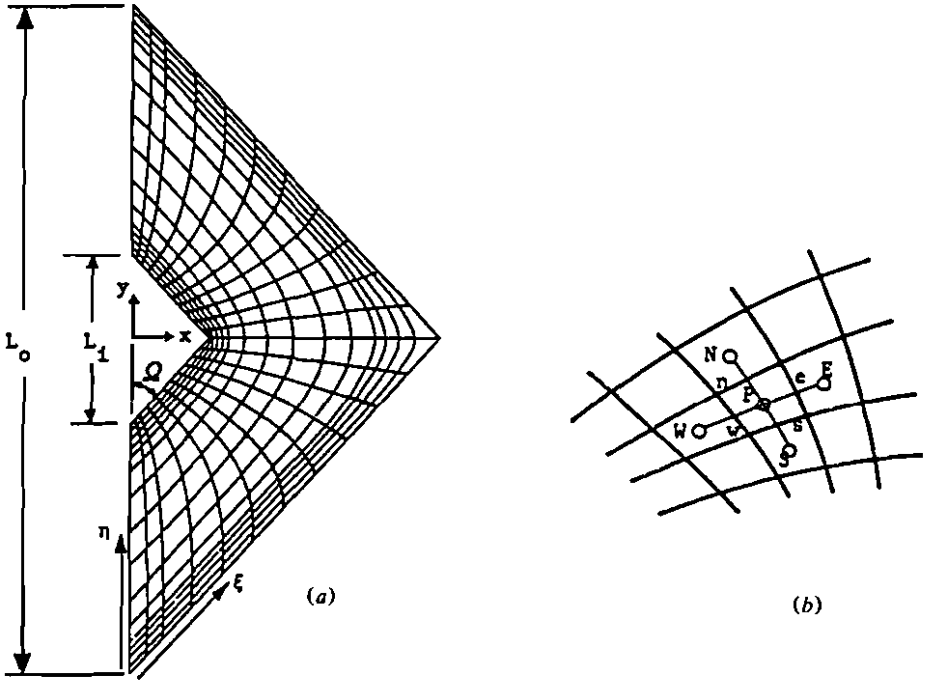

Fig. 1 (*a*) Physical domain and an sample generated grid. (*b*) A typical control volume.

aforementioned assumptions, the nondimensional mass, momentum, and energy equations become

$$\frac{\partial U}{\partial X} + \frac{\partial V}{\partial Y} = 0 \tag{2}$$

$$U\frac{\partial U}{\partial X} + V\frac{\partial U}{\partial Y} = -\frac{\partial P}{\partial X} + \frac{\partial^2 U}{\partial X^2} + \frac{\partial^2 U}{\partial Y^2} \tag{3}$$

$$U\frac{\partial V}{\partial X} + V\frac{\partial V}{\partial Y} = -\frac{\partial P}{\partial Y} + \frac{\partial^2 V}{\partial X^2} + \frac{\partial^2 V}{\partial Y^2} + \frac{\mathrm{Ra}\,\theta}{\mathrm{Pr}} \tag{4}$$

$$U\frac{\partial \theta}{\partial X} + V\frac{\partial \theta}{\partial Y} = \frac{1}{\mathrm{Pr}}\left\{\frac{\partial^2 \theta}{\partial X^2} + \frac{\partial^2 \theta}{\partial Y^2}\right\} \tag{5}$$

where the dimensionless variables used have been defined in the nomenclature.

The problem is solved using the no-slip boundary conditions along the walls. The hot inner and cold outer walls are maintained at nondimensional uniform temperatures of 1 and 0, respectively. Due to symmetry around the Y axis, computations are performed on the right portion of the physical domain. The U velocity and the gradients of the remaining variables are set to zero along the symmetry line.

SOLUTION PROCEDURE

For a rhombic annulus, since the boundaries do not lie along Cartesian coordinates, a curvilinear coordinate system is the most appropriate method to use. The solution to the system of equations given by Eqs. (2)–(5) is generally obtained on a staggered grid to avoid checkerboard pressure and velocity fields. Thus, three sets of grid positions (one each for the two components of velocity and the third for pressure) and associated metric quantities have to be calculated and stored. It is therefore desirable to use a nonstaggered grid arrangement that will suppress checkerboard pressure and velocity fields. In this paper, a nonstaggered grid arrangement is used, and the method of Rhie and Chow [14] that embodies the Semi-implicit method for pressure linked equations (SIMPLE) algorithm of Patankar [15] is used to suppress oscillatory checkerboard fields.

A brief description of the various steps in the calculation process is given next. These steps are grid generation, discretization of the conservation equations, and the solution algorithm. Additional details are documented elsewhere [14–17].

Grid Generation

The curvilinear grid is generated by solving the following system of equations [18]:

$$\alpha\frac{\partial^2 X}{\partial \xi^2} - 2\beta\frac{\partial^2 X}{\partial \xi\,\partial \eta} + \gamma\frac{\partial^2 X}{\partial \eta^2} = 0 \qquad \alpha\frac{\partial^2 Y}{\partial \xi^2} - 2\beta\frac{\partial^2 Y}{\partial \xi\,\partial \eta} + \gamma\frac{\partial^2 Y}{\partial \eta^2} = 0 \tag{6}$$

where $\xi(X,Y)$ and $\eta(X,Y)$ are the curvilinear coordinates (Fig. 1*a*). The metric quantities α, β, and γ are defined in the nomenclature.

Central differences are used to discretize Eq. (6). The resulting system of equations is solved iteratively and gives (X,Y) values at uniform (ξ,η) values. A sample of a generated grid network is shown in Fig. 1*a*.

Discretization of the Conservation Equations

The conservation equations, Eqs. (2)–(5), for a general variable ϕ can be written in the following general form in curvilinear coordinates:

$$\frac{\partial}{\partial\xi}\left\{G_1\phi - \left(\frac{\Gamma^\phi}{J}\right)\left(\alpha\frac{\partial\phi}{\partial\xi} - \beta\frac{\partial\phi}{\partial\eta}\right)\right\} + \frac{\partial}{\partial\eta}\left\{G_2\phi - \left(\frac{\Gamma^\phi}{J}\right)\left(\gamma\frac{\partial\phi}{\partial\eta} - \beta\frac{\partial\phi}{\partial\xi}\right)\right\} = S^\phi J \tag{7}$$

where S^ϕ is the source term, Γ^ϕ is the diffusion coefficient, and G_1/J and G_2/J are the contravariant velocity components (see the nomenclature).

The control volume approach is adopted here. With this approach the domain is subdivided into a number of control volumes, each associated with a grid point. The finite difference form is obtained by integrating Eq. (7) over the control volume shown in Fig. 1*b*. This leads to an integral balance equation that is reduced to an algebraic equation by expressing the dependent variable ϕ and its derivatives in terms of the grid point values using the power law scheme of Patankar [15]. The resulting discretization equation can be written as

$$a_P^\phi\phi_P = a_E^\phi\phi_E + a_W^\phi\phi_W + a_N^\phi\phi_N + a_S^\phi\phi_S + b_o^\phi + b_{no}^\phi + b_P^\phi \tag{8}$$

where all terms are defined in the nomenclature.

The unknown pressure field is obtained using the SIMPLE algorithm, in which pressure and velocity are defined by

$$P = P^* + P' \qquad U = U^* + U' \qquad V = V^* + V' \tag{9}$$

where P^*, U^*, and V^* are currently available estimates for pressure and velocity and P', U', and V' are the pressure and velocity corrections, respectively. A pressure-correction equation is derived by combining Eq. (9) with the momentum and continuity equations. The equation has the same form as that given by Eq. (8).

To suppress spurious oscillations in the predicted solutions, Rhie and Chow [14] added the following correction term to G^* in the source term of the pressure-correction equation:

$$(G_1^*)_e = \overline{G_1^*} + \overline{B}\left\{\frac{(P_E - P_P)}{\delta\xi} - \overline{\frac{\partial P}{\partial\xi}}\right\} \tag{10}$$

where the overbar indicates that the results are obtained by linear interpolation between grid nodes and B depends on the metric quantities and the coefficients. The system of equations is solved by a line-by-line Thomas algorithm described in greater detail in Patankar [15]. The overall solution procedure is given in Acharya and Moukalled [17].

Numerical Accuracy

To determine a suitable grid size, the computed profiles of velocity, temperature, and local Nusselt number were compared for a number of grid sizes. A final grid size of 42×32 grid points was chosen for this study. The grid points were unevenly distributed over the domain with denser clustering near the walls, where higher gradients are expected. Comparison of the solution on a 42×32 grid (1344 grid points) with the solution on a 62×42 grid (2604 grid points) revealed that the maximum differences were less than 2% in the peak Nusselt number value and less than 1.8% in the peak midheight horizontal velocity. Conservation of mass, momentum, and energy was found to be satisfied to within 0.01% in each control volume.

RESULTS AND DISCUSSION

The main parameters of interest in this study are the dimensionless enclosure gap E_g, the rhombic angle Ω, the Rayleigh number Ra, and the Prandtl number Pr. Parameter values considered are four different values of the enclosure gap ($E_g = 0.875, 0.75, 0.5, 0.25$), seven Rayleigh numbers in the range 10^3–10^7, and three rhombic angles ($\Omega = 10°, 20°, 30°$). Air is considered to be the working fluid, and therefore, the Prandtl number is fixed at 0.71.

Streamlines and Isotherms

Representative streamline maps are shown in Figs. 2–6 along with corresponding isotherm distributions. Results presented are for $\mathrm{Ra} = 10^4$–10^7, $\Omega = 30°$, and $E_g = 0.875$–0.25. The maximum stream function values ($|\psi_{max}|$) are shown in Table 1.

Inspection of the streamlines depicted in Figs. 2–6 shows that, in general, the flow follows the contour of the rhombus. The dominant feature of the flow field is a recirculating eddy with the fluid moving upward adjacent to the inner hot wall and along the symmetry axis, and downward adjacent to the outer cold wall. The eye of the recirculation is situated in the upper portion of the enclosure, where the strong vortices are located. This is easily seen for high values of the enclosure gap (Figs. 2 and 3). With increasing Ra, the eye moves further upward and outward toward the outer wall. The velocities at the bottom of the enclosure are very low compared with the velocities at the middle and top regions. The strength of the convective cells increases with the magnitude of the buoyancy force or Ra. Thus, as seen later, the convective heat transfer also increases with Ra.

At the lower Rayleigh numbers ($\mathrm{Ra} = 10^3$) studied and for all the dimensionless gaps considered, a relatively weak convective flow exists in the cavity, and the

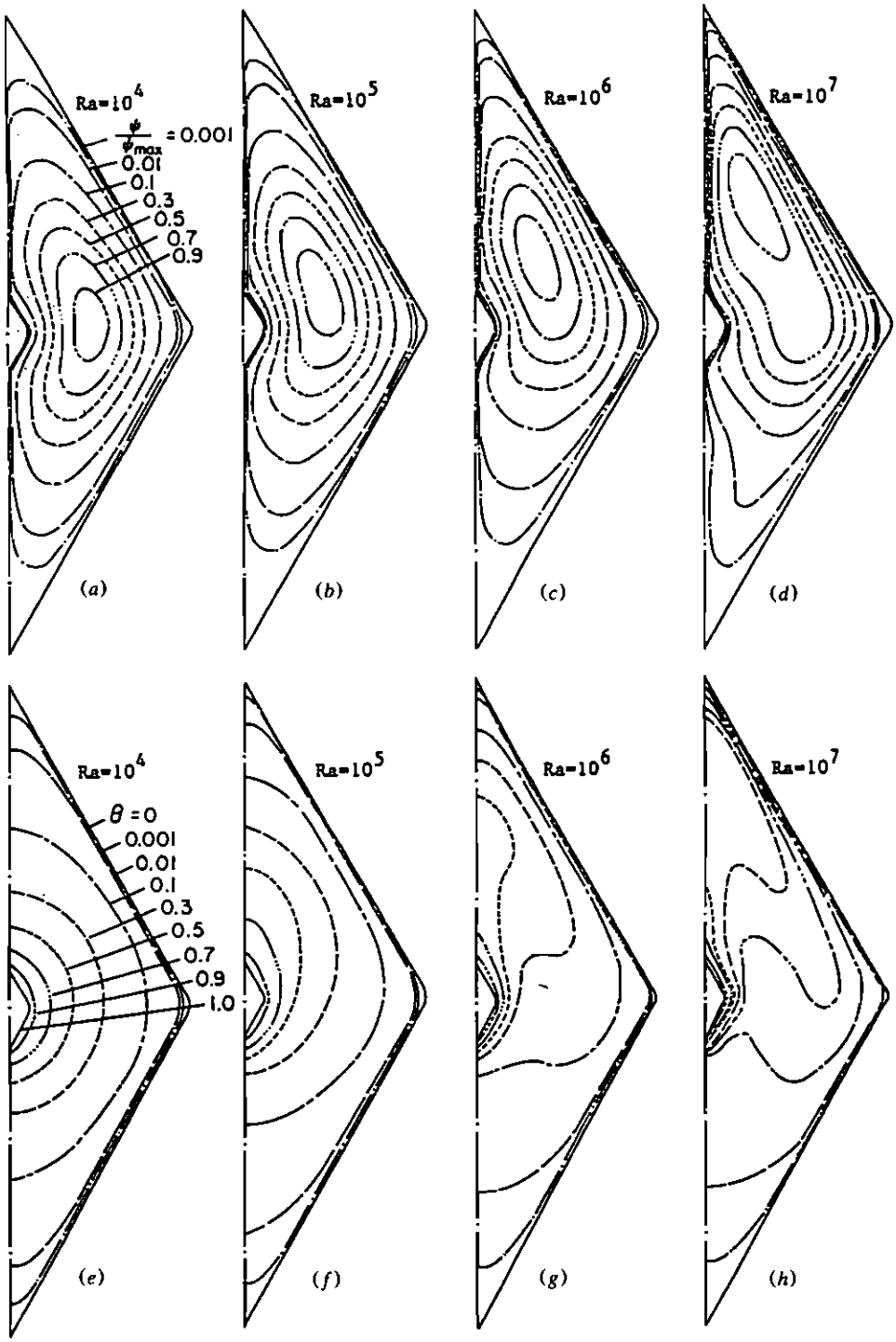

Fig. 2 Streamline and isotherm plots for $E_g = 0.875$, $\Omega = 30°$.

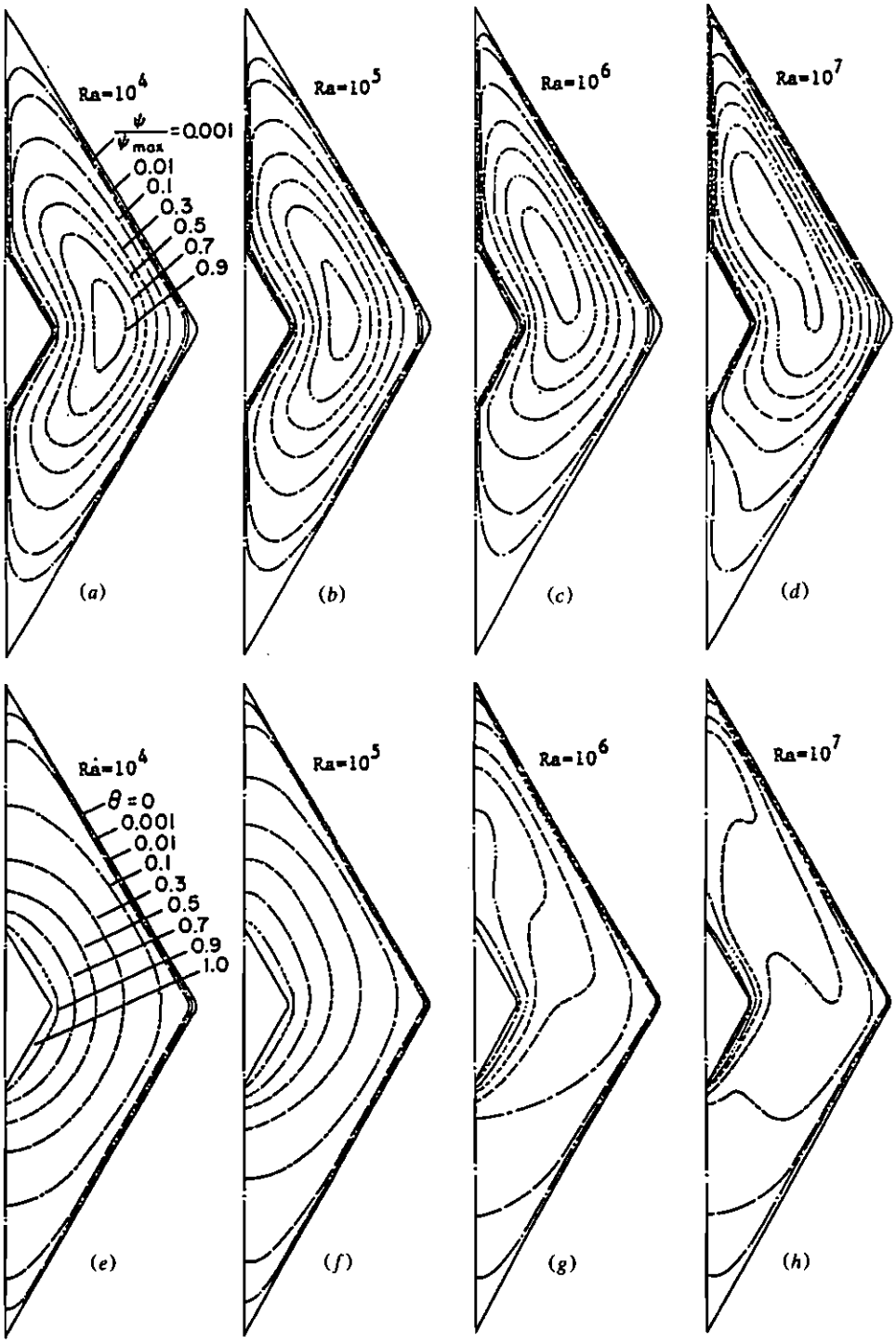

Fig. 3 Streamline and isotherm plots for $E_g = 0.75$, $\Omega = 30°$.

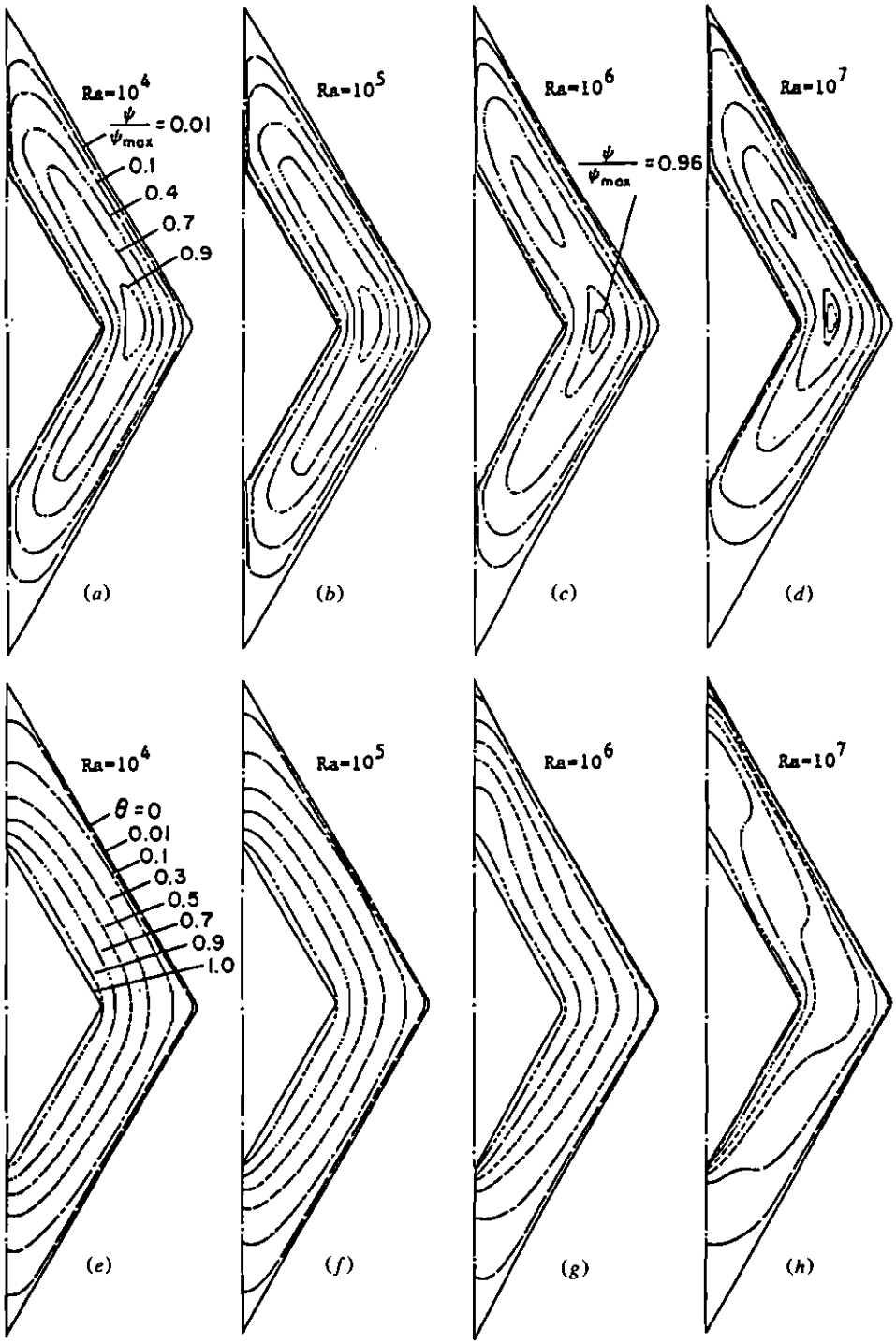

Fig. 4 Streamline and isotherm plots for $E_g = 0.5$, $\Omega = 30°$.

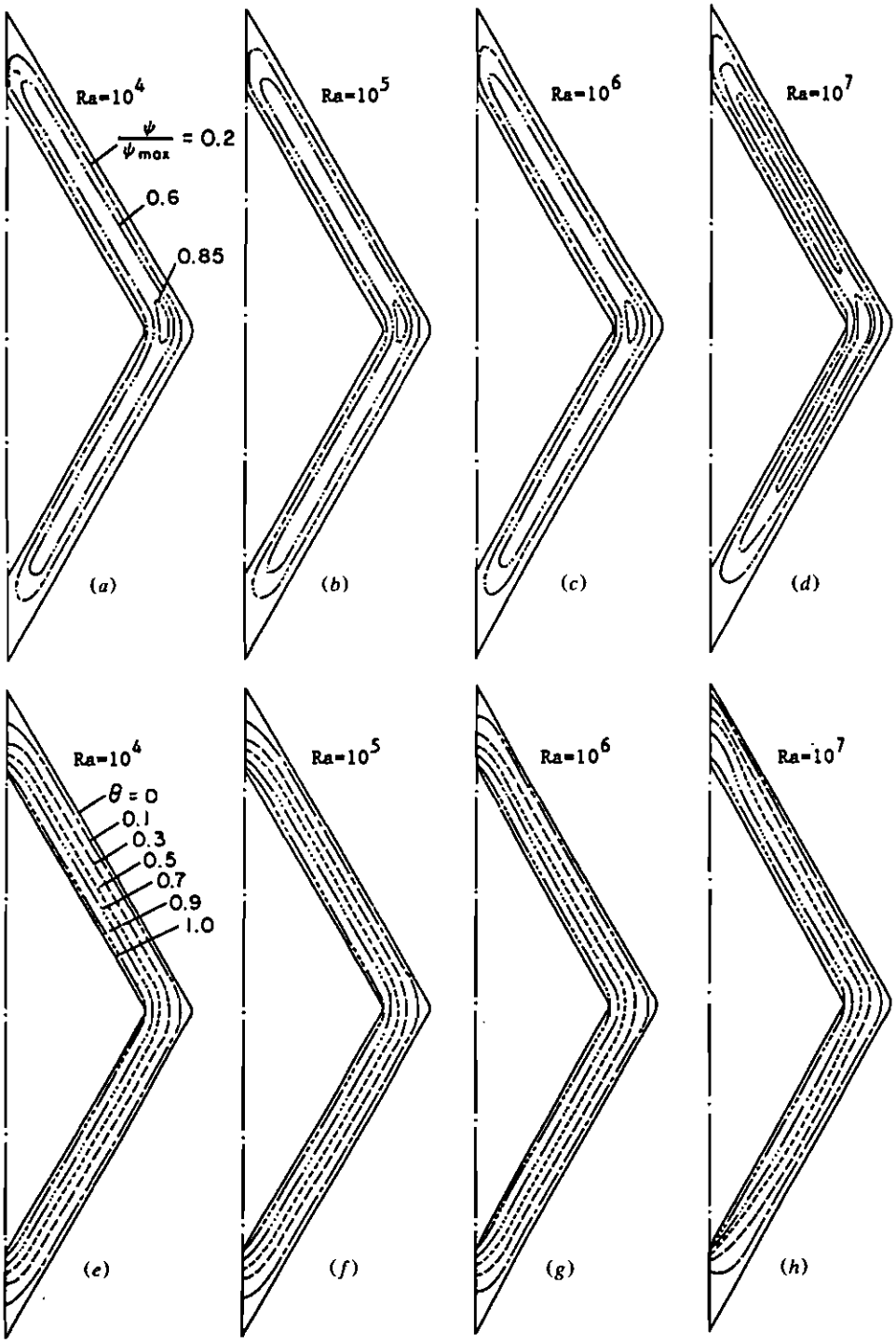

Fig. 5 Streamline and isotherm plots for $E_6 = 0.25$, $\Omega = 30°$.

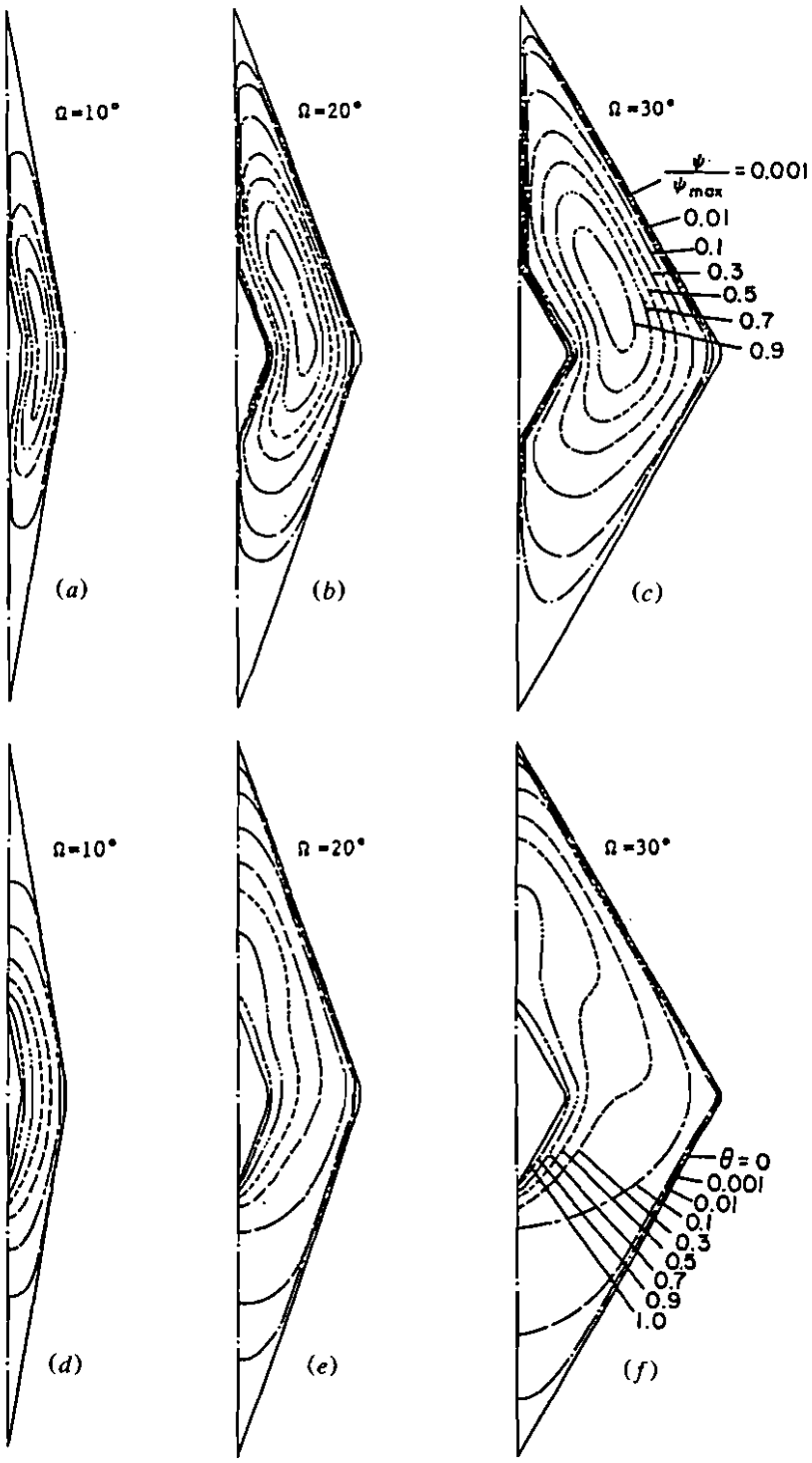

Fig. 6 Streamline and isotherm plots for $E_g = 0.75$, Ra = 10^6.

Table 1 Maximum Absolute Values of the Stream Function

	Value of E_g									
	0.875	0.75			0.5			0.25		
Ra	30°	10°	20°	30°	10°	20°	30°	10°	20°	30°
10^3	0.0347	0.00103	0.0079	0.0246	0.00031	0.0024	0.00754	0.00004	0.0003	0.00096
10^4	0.347	0.0103	0.079	0.246	0.00306	0.0237	0.0754	0.00038	0.003	0.0096
10^5	3.22	0.103	0.788	2.37	0.0306	0.237	0.753	0.0038	0.03	0.0955
10^6	15.4	1.03	7.02	14.2	0.306	2.36	7.12	0.038	0.295	0.952
10^7	40.2	—	—	39.1	—	—	35.7	—	—	8.71

flow patterns and temperature distributions tend to be symmetrical across the horizontal diagonal of the enclosure. At higher Ra, the isotherm and flow patterns become asymmetrical about the horizontal diagonal, and as noted above, the eye of the recirculating eddy moves upwards and outward toward the cold wall. This behavior is particularly noticeable at higher E_g values (0.875 and 0.75) and is due to the significantly larger area of the cold surface relative to the area of the hot surface. Below the horizontal diagonal the cooled surface promotes stratification in the lower half, and above the diagonal the hot surface promotes stratification in the upper half. Since for higher E_g values, the lower half is dominated by the much larger cold surface area, there is significant temperature stratification in the lower half, as seen from Figs. 2*g*, 2*h*, 3*g*, and 3*h*. Because of the thermal stratification in the lower half, the flow cannot easily penetrate the lower region, and as seen in Figs. 2*c*, 2*d*, 3*c*, and 3*d*, the flow in this region is essentially stagnant or very weak. In the upper half, due to the relatively lower proportion of the hot surface area, stratification is not significant, and a strong recirculating flow is obtained.

As E_g is decreased, and the proportion of the hot to the cold surface area approaches unity, the aforedescribed stratification effects in the lower half become less noticeable. In Fig. 5, where $E_g = 0.25$, the stratification in the lower half has virtually disappeared, and the flow pattern in the upper and lower halves look similar.

At higher Ra, the recirculating flow exhibits two vortex cores within one overall large rotating eddy (see Figs. 4*c*, 4*d*, and 5*d*). These two inner vortices rotate in the clockwise direction. For the largest enclosure gap value, a single vortex core is observed.

The strength of the flow (indicated by $|\psi_{max}|$) decreases with decreasing enclosure gap value, as expected. This is seen in Table 1 and is due to the greater viscous effects of the added surface area. For the same reasons, at constant enclosure gap values, the strength of the flow decreases with decreasing rhombic angle. In addition, Table 1 indicates that, as long as the heat transfer mechanism is dominated by conduction, the maximum stream function value increases almost linearly with Ra. However, once convection is dominant, this linear relation no longer holds.

At Ra = 10^7, and for $E_g = 0.5$, 0.75, and 0.875, the convective flow strength is significant, and the isotherm plots in Figs. 2*h*, 3*h*, and 4*h* clearly show the boundary layer behavior on the lower part of the heated surface and the upper part of the cooled enclosure surface. The boundary layer along the inner wall rises up

from the upper region of the inner body and forms a thermal plume. This can be seen as isotherms move rapidly away from the inner wall near the top.

The effect of the rhombic angle on flow and temperature fields is shown in Fig. 6 for $E_g = 0.75$ and $Ra = 10^6$. Streamline and isotherm plots in this figure indicate that increasing the rhombic angle increases convection. Moreover, the eye of the recirculating eddy is seen to move upward and outward with increasing Ω (Figs. 6*a*–6*c*), implying stronger convection as a result of the increase in the available convection area. For the same reason, with increasing Ω, the isotherms in Figs 6*d*–6*f* become more asymmetrical around the horizontal diagonal of the rhombus.

Velocity and Temperature Profiles

Figure 7 shows vertical velocity profiles at the cavity midheight for $\Omega = 30°$, $E_g = 0.875$, and $Ra = 10^4$, 10^5, 10^6, and 10^7. The peak velocities increase with increasing Ra and occur close to the walls, as expected. The velocity profiles are steeper near the hot wall than near the cold wall. The magnitude of the velocity is very small at low Ra, indicating a heat transfer mode of weak convection and dominant conduction. The maximum vertical velocity along the horizontal diagonal increases as the enclosure gap value increases from 0.25 to 0.875, as expected.

The corresponding midheight temperature profiles are shown in Fig. 8. For high values of Ra, the near-wall region is characterized by a thermal boundary layer, and the temperature profile is characterized by sharp gradients near the hot and cold walls and higher values near the hot wall. The variation in temperature is

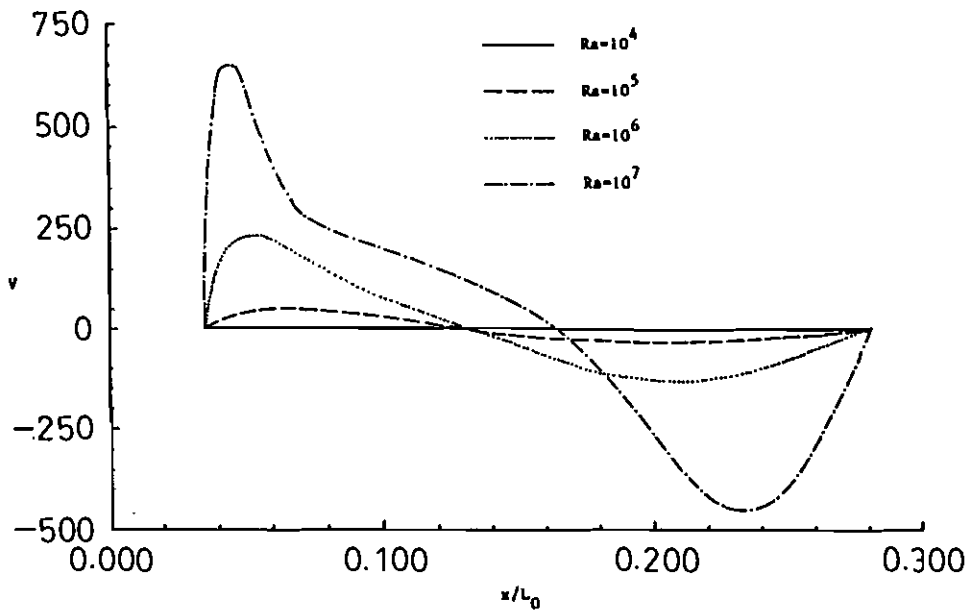

Fig. 7 Midheight vertical velocity profiles for $E_g = 0.875$, $\Omega = 30°$.

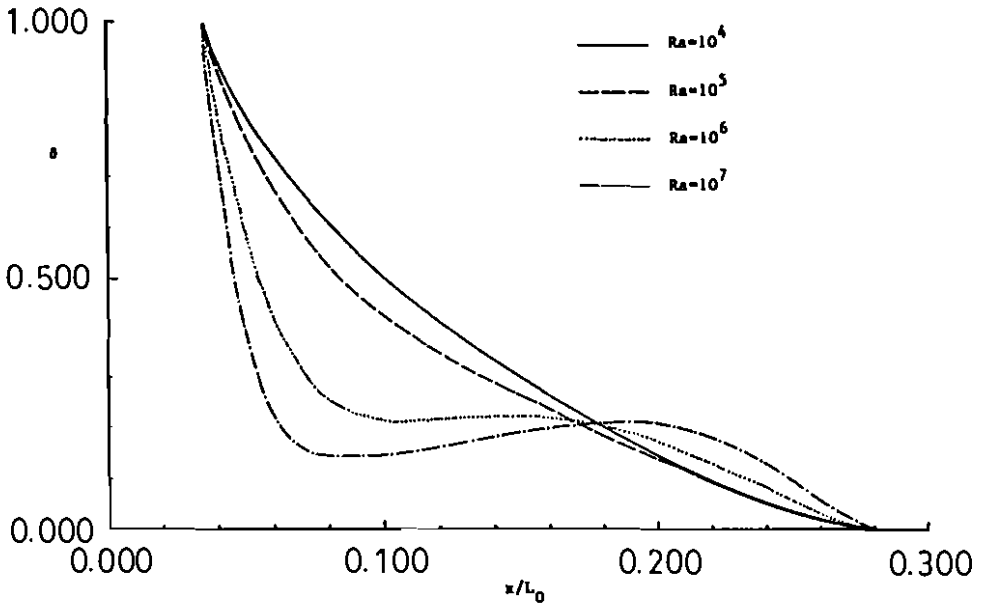

Fig. 8 Midheight temperature profiles for $E_g = 0.875$, $\Omega = 30°$.

almost linear at low Ra, indicating conduction as the dominant heat transfer mode. By comparing curves for $E_g = 0.875$ (Fig. 8) and $E_g = 0.25$ (not shown), at the same Ra, it is clear that the temperature distortion is stronger at higher enclosure gap values due to the stronger convective flow.

Nusselt Numbers

The local and average heat transfer coefficients at the inner and outer walls were computed using the following definitions:

$$h_i = -\frac{k(\partial T/\partial n)|_i}{(T_i - T_o)} \qquad h_o = -\frac{k(\partial T/\partial n)|_o}{(T_i - T_o)} \tag{11}$$

$$\overline{h_i} = \frac{Q_{conv}}{A_i(T_i - T_o)} \qquad \overline{h_o} = \frac{Q_{conv}}{A_o(T_i - T_o)} \tag{12}$$

where n denotes the normal distance from the wall, Q_{conv} is the total convection heat transfer at the surface

$$= \int_i -k\frac{\partial T}{\partial n}\bigg|_i ds \quad \text{or} \quad \int_o -k\frac{\partial T}{\partial n}\bigg|_o ds$$

and A_i and A_o are the heat transfer areas along the inner and outer walls,

respectively. The Nusselt number is defined in the conventional manner as $Nu_i = h_i/k$ along the inner wall and $Nu_o = h_o L_o/k$ along the outer wall. Since $A_i = L_i/\cos\Omega$ and $A_o = L_o/\cos\Omega$, it follows that $\overline{Nu_i} = \overline{Nu_o}$. In light of this, there is no need to give separate attention to $\overline{Nu_i}$ and $\overline{Nu_o}$, and attention will subsequently be focused on $\overline{Nu}$.

The local Nusselt number distributions along the hot and cold walls are presented for enclosure gap values of 0.875 and 0.5 in Figs. 9 and 10, respectively. Values are plotted as a function of s/s_{max}, where s is distance along the wall measured from its lowest point and s_{max} is the maximum possible length.

For $E_g = 0.875$ along the inner hot wall, the Nusselt number peaks near the bottom region ($s = 0$) of the hot wall. The cooled fluid from the cold wall is transported by the clockwise eddy toward the lower regions of the hot wall, and the largest temperature gradients and Nusselt numbers therefore occur in the leading regions of the hot wall ($s = 0$). This behavior is particularly accentuated at higher Ra, where the thermal boundary layer can clearly be seen on the hot inner wall (Fig. 2*h*). At lower Ra (Fig. 2*e*) the isotherm pattern is more symmetrical along the lower and upper parts, and the Nu distribution is correspondingly more uniform.

Along the outer cooled wall, at lower Ra, the profile is nearly symmetrical, reflecting the effects of the symmetrical flow pattern and isotherms shown in Figs. 2*a* and 2*e*. A local maximum is observed along the upper region ($s/s_{max} > 0.5$) and the lower region ($s/s_{max} < 0.5$) The upper maximum is due to the hot fluid from the inner wall rising upward and impinging on the cold upper wall. The local maximum along the lower wall is due to the impingement and deflection of the downward descending fluid by the lower portion of the cold wall. Since this fluid is

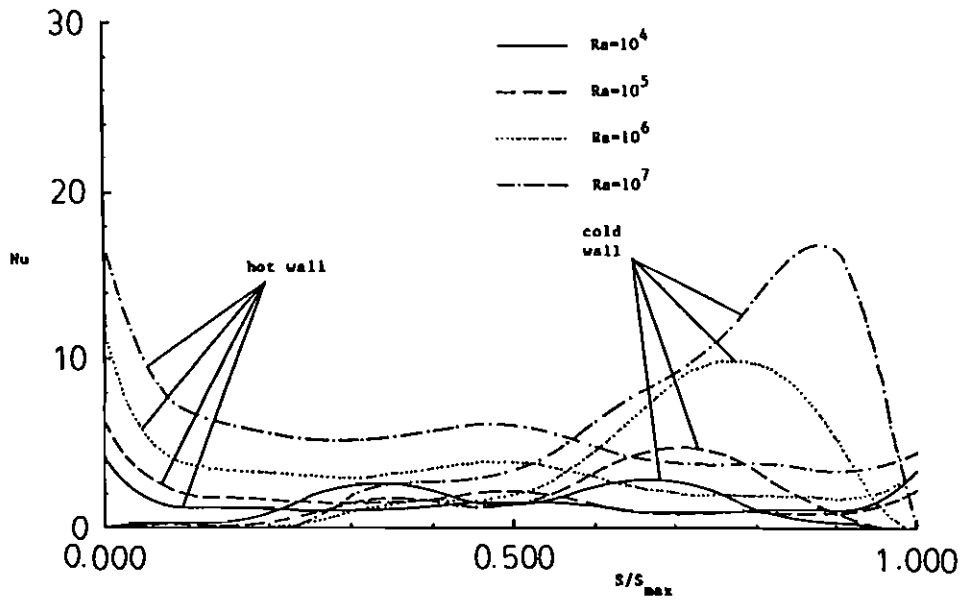

Fig. 9 Local Nusselt number distribution along the hot and cold walls for $E_g = 0.875$, $\Omega = 30°$.

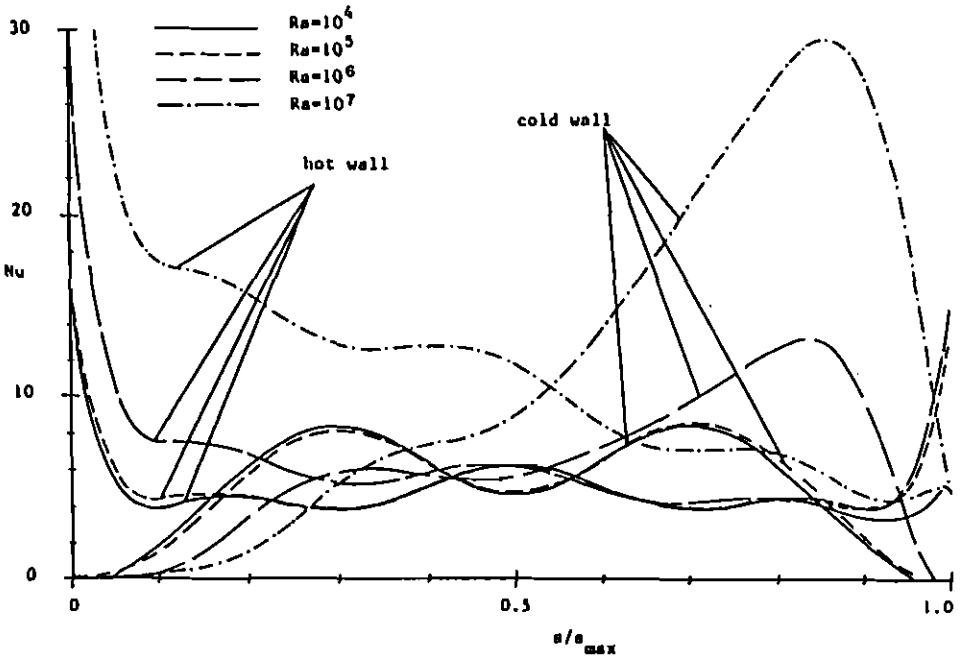

Fig. 10 Local Nusselt number distribution along the hot and cold walls for $E_g = 0.5$, $\Omega = 30°$.

cooler than the upward impinging fluid on the upper cold wall, the corresponding Nusselt number peak for $s/s_{max} < 0.5$ is lower. As Ra increases, the lower portion is increasingly thermally stratified, the downward descending flow penetrates the lower region to a lesser degree, and the maximum Nu in the lower region ($s/s_{max} < 0.5$) correspondingly decreases. On the other hand, with increasing Ra, the strength of the convective flow increases in the upper portion of the enclosure (compare Figs. 2*a*–2*d*), and consequently, the Nu peak increases along the upper cold wall.

For $E_g = 0.5$ (Fig. 10), the Nu profiles along the hot and cold walls show behavior similar to that in Fig. 9. The profile is nearly symmetrical at lower Ra ($Ra = 10^4$ and 10^5). At $Ra = 10^6$ and 10^7 the convective effects become important, and the profiles become skewed.

The average Nu for all cases studied are given in Table 2. At lower Ra the overall heat transfer appears to be strongly dominated by conduction. Beyond a certain critical Ra, convection effects become important on the overall heat transfer. The critical Ra increases with decreasing E_g; at $E_g = 0.875$ the critical Ra is between 10^4 and 10^5, while at $E_g = 0.25$ it appears to be close to $Ra = 10^6$. Below this critical Ra, convection effects are weak, and although the velocity, temperature, and heat transfer profiles show mild distortions due to the convective flow, these effects are not strong enough to substantially change the overall heat transfer. For Ra less than the critical value, the overall heat transfer is much larger at lower enclosure gap values because of the increased heat conduction contribution at low E_g values (at low E_g values, gap width for the same ΔT is smaller). The

same is true for lower rhombic angle values and explains the large variation in the values obtained with the rhombic angle. The highest $\overline{Nu}$ value of 37.91 is found for the lowest enclosure gap and rhombic angle and the highest Ra. Also, the lowest $\overline{Nu}$ of 1.4 is attained at the lowest Ra and the highest enclosure gap and rhombic angle. At constant enclosure gap values, the $\overline{Nu}$ decreases with increasing rhombic angle, and increases with increasing Ra due to the increase in the magnitude of the buoyancy forces. When Ra is held constant, $\overline{Nu}$ increases with decreasing E_g and/or rhombic angle. As mentioned earlier, this is due to the increase in conduction heat transfer. Further, when conduction is the dominant heat transfer mode, $\overline{Nu}$ predictions are almost insensitive to the variation in Ra.

The values listed in Table 2 represent the average of the contributions from the lower and upper parts of each isothermal wall. For the cold wall, where convection is important (convection is stronger for larger Ra, larger E_g, and higher Ω), the upper half contributes more to the total heat transfer. This is expected, since as noted earlier, due to thermal stratification in the lower half, the velocities above the diagonal midplane are significantly larger, and consequently, the heat transfer along the upper part of the cold wall is larger. Note that the difference in contributions from the upper and lower portions of the cold wall can be quite significant. For example, at $Ra = 5 \times 10^5$ and $E_g = 0.875$, heat transfer at the upper cold wall is nearly 9 times that at the lower cold wall. As E_g decreases, and convective effects become less important, the contributions from the upper and lower parts of the cold wall approach each other.

Along the hot wall, similar observations can be made. Where convection is important, the lower half of the hot wall, which is first washed by the flow descending the cold wall, has higher heat transfer rates compared with the upper part of the hot wall. As E_g and Ra decrease and convection effects diminish, the contributions from each half of the hot wall approach each other.

CONCLUDING REMARKS

A numerical study has been conducted of natural convection between two concentric pipes of rhombic cross sections, with the inner pipe heated and the outer pipe cooled. The results indicate that for a given dimensionless gap between

Table 2 Average Nusselt Number Values

	Value of E_g									
	0.875	0.75			0.5			0.25		
Ra	30°	10°	20°	30°	10°	20°	30°	10°	20°	30°
10^3	1.40	4.90	2.89	2.23	13.18	6.92	5.08	37.91	20.64	14.36
10^4	1.40	4.90	2.89	2.23	13.18	6.92	5.08	37.91	20.64	14.41
10^5	1.69	4.90	2.89	2.37	13.18	6.94	5.08	37.91	20.64	14.41
5×10^5	2.75	4.90	3.49	3.27	13.18	6.95	5.42	37.91	20.64	14.41
10^6	3.24	4.90	4.01	4.49	13.18	6.96	5.94	37.91	20.65	14.42
5×10^6	4.62	5.68	6.39	6.92	13.20	7.10	8.85	37.91	20.65	14.51
10^7	5.41	6.66	8.21	8.10	13.24	10.77	11.55	37.91	20.65	15.24

the two pipes, E_g, there is a critical Ra below which conduction is the dominant mode of heat transport. This critical Ra decreases with increasing E_g and increasing rhombic angle Ω. Convection promotes thermal stratification below the horizontal diagonal, leading to an increasingly stagnant flow with increasing Ra in the lower half of the enclosure. As Ra is increased, the eye of the recirculating eddy moves upward and outward toward the upper portion of the cold wall. As the gap between the two pipes decreases, the added surface area reduces the flow strength, the thermal stratification, and the asymmetry between the upper and lower halves. At high Ra, boundary layer behavior is observed along the lower half of the inner hot wall and the upper half of the outer cold wall. Correspondingly, the Nu profiles exhibit a characteristic boundary layer peak along the lower part of the inner wall and a maximum along the upper part of the outer wall. Below the critical Ra, where conduction is the dominant mode of heat transport, the average Nu increases with decreasing dimensionless gap width and rhombic angle. Above the critical Ra, Nu increases with increasing Ra and decreasing dimensionless gap values.

REFERENCES

1. S. Ostrach, Natural Convection in Enclosures, *ASME J. Heat Transfer*, vol. 110, pp. 1175–1190, 1988.
2. T. H. Kuehn and R. J. Goldstein, An Experimental and Theoretical Study of Natural Convection in the Annulus between Horizontal Concentric Cylinders, *J. Fluid Mech.*, vol. 74, pp. 695–709, 1976.
3. A. Castrejon and D. B. Spalding, An Experimental and Theoretical Study of Transient Free-Convection Flow between Horizontal Concentric Cylinders, *Int. J. Heat Mass Transfer*, vol. 31 pp. 273–284, 1988.
4. R. Kumar, Study of Natural Convection in Horizontal Annuli, *Int. J. Heat Mass Transfer*, vol. 31, pp. 1137–1148, 1977.
5. P. M. Kolesnikov and V. I. Bubnovich, Non-Stationary Conjugate Free-Convective Heat Transfer in Horizontal Cylindrical Coaxial Channels, *Int. J. Heat Mass Transfer*, vol. 31, pp. 1149–1156, 1988.
6. C. H. Cho, K. S. Chang, and K. H. Park, Numerical Simulation of Natural Convection in Concentric and Eccentric Horizontal Cylindrical Annuli, *ASME J. Heat Transfer*, vol. 104, pp. 524–630, 1982.
7. J. Prusa and L. S. Yao, Natural Convection Heat Transfer between Eccentric Horizontal Cylinders, *ASME J. Heat Transfer*, vol. 105, pp. 108–116, 1983.
8. C. J. Ho and Y. H. Lin, Natural Convection Heat Transfer of Cold Water within an Eccentric Horizontal Cylindrical Annulus, *ASME J. Heat Transfer*, vol. 110, pp. 894–900, 1988.
9. D. Naylor, H. M. Badr, and J. D. Tarasuk, Experimental and Numerical Study of Natural Convection between Two Eccentric Tubes, *Int. J. Heat Mass Transfer*, vol. 32, pp. 171–181, 1989.
10. K. S. Chang, Y. H. Won, and C. H. Cho, Patterns of Natural Convection around a Square Cylinder Placed Concentrically in a Horizontal Cylinder, *ASME J. Heat Transfer*, vol. 105, pp. 273–280, 1983.
11. J. H. Lee and T. S. Lee, Natural Convection in the Annuli between Horizontal Confocal Elliptic Cylinders, *Int. J. Heat Mass Transfer*, vol. 24, no 10, pp. 1739–1742, 1981.
12. N. Seki, S. Fukusako, and A. Yamaguchi, An Experimetal Study of Free Convective

Heat Transfer in a Parallelogrammic Enclosure, *ASME J. Heat Transfer*, vol. 105, pp. 433–439, 1983.
13. R. D. Boyd, Steady Natural Convection Heat Transfer Experiments in a Horizontal Annulus for the United States Spent Fuel Shipping Cask Technology Program, Sandia National Lab. Rept. SAND-80-1057, 1981.
14. C. M. Rhie and W. L. Chow, Numerical Study of the Turbulent Flow Past an Airfoil with Trailing Edge Separation, *AIAA J.*, vol. 21, pp. 1525–1532, 1983.
15. S. V. Patankar, *Numerical Heat Transfer and Fluid Flow*, Hemisphere, New York, 1980.
16. F. Moukalled, Adaptive Grid Solution Procedure for Elliptic Flows, Ph.D. thesis, Louisiana State University, 1987.
17. S. Acharya and F. H. Moukalled, Improvements to Incompressible Flow Calculation on a Nonstaggered Curvilinear Grid, *Numer. Heat Transfer, Part B*, vol. 15, pp. 131–152, 1989.
18. J. F. Thompson, *Numerical Grid Generation*, North-Holland, Amsterdam, 1982.

Received 31 July 1991
Accepted 12 May 1992

Address correspondence to S. Acharya.